Journal of Power Sources 626 (2025) 235773

Contents lists available at ScienceDirect

Journal of Power Sources

journal homepage: www.elsevier.com/locate/jpowsour

Simultaneously improving sodium ionic conductivity and dendrite behavior of NaSICON ceramics by grain-boundary modification

Limin Liu [a,e,1], Qianli Ma [b,**,1], Xiaoliang Zhou [a,e,*], Ziming Ding [c,d], Daniel Grüner [b], Christian Kübel [c,d], Frank Tietz [b]

[a] Southwest Petroleum University, College of Chemistry and Chemical Engineering, Chengdu, 610500, PR China
[b] Forschungszentrum Jülich GmbH, Institute of Energy Materials and Devices (IMD), 52425, Jülich, Germany
[c] Technische Universität Darmstadt, 64289, Darmstadt, Germany
[d] Institut of Nanotechnology (INT), Karlsruhe Nano Micro Facility (KNMFi), and Helmholtz Institut Ulm (HIU), Karlsruhe Institute of Technology (KIT), 76344, Eggenstein-Leopoldshafen, Germany
[e] Tianfu Yongxing Laboratory, Chengdu, 610213, PR China

HIGHLIGHTS

- NZSP is modified by adding 2.5 mol% NLP, resulting in σ_{total} of 7.1 mS cm^{-1} at RT.
- The effect of NLP is to reinforce the grain-boundary of NZSP.
- NZSP:NLP shows high robustness against Na dendrite in Na.|NZSP:NLP|Na cells.
- The CCD is up to 22 mA cm^{-2}, and long-term cycling is up to 10 mA cm^{-2}.
- The cells show the loop of polarizations and short-circuits after dendrite.

ARTICLE INFO

Keywords:
Solid-state sodium battery
NaSICON
Grain-boundary modification
Dendrite behavior
Cryogenic STEM

ABSTRACT

Developing highly conductive and reliable solid-electrolytes (SEs) is still important for the advancement of solid-state sodium batteries. NaSICON-type polycrystalline SEs exhibit the dominance of grain-boundary resistance to the total resistance, which is mainly due to the thermal expansion anisotropy of NaSICON-type lattices. In this study, we modify the grain boundaries of NaSICON-type $Na_{3.4}Zr_2Si_{2.4}P_{0.6}O_{12}$ (NZSP) by adding 2.5 mol% $Na_3LaP_2O_8$ (NLP) to counteract the effect of thermal expansion anisotropy. NLP does not serve as a sintering aid for NZSP because the sintering temperature and relative density of NZSP is not changed. The total conductivity of modified NZSP increases to 7.1 mS cm^{-1} at 25 °C, surpassing other reported polycrystalline oxide SEs. The critical current density of Na | modified NZSP | Na symmetric cells increases to 22 mA cm^{-2}. The cells can survive under long-term galvanostatic cycling up to 10 mA cm^{-2}, indicating the unprecedented dendrite tolerance. Remarkably, the main failure mode in these cells shifts from Na-dendrite short-circuiting to the loop of substantial polarizations and short-circuits.

1. Introduction

The escalating demand for batteries, coupled with the limited and uneven distribution of resources, is continuously raising the cost of lithium-based batteries [1]. Hence, sodium-based batteries are gaining increasing attention due to their comparable physicochemical properties, abundant resources as well as the lower costs of raw materials [2–4]. Similar to their lithium-counterparts, sodium-based batteries with solid-state design (SSNBs) are considered as the next-generation batteries, offering improvements in long-term stability, safety, and energy density compared to conventional liquid electrolyte-based batteries [5–9].

* Corresponding author. Southwest Petroleum University, College of Chemistry and Chemical Engineering, Chengdu, 610500, PR China.
** Corresponding author.
E-mail addresses: q.ma@fz-juelich.de (Q. Ma), xlzhou_swpu@sina.com (X. Zhou).
[1] These authors contributed equally.

https://doi.org/10.1016/j.jpowsour.2024.235773
Received 17 September 2024; Received in revised form 16 October 2024; Accepted 2 November 2024
Available online 13 November 2024

Developing highly conductive and reliable solid electrolytes (SEs) is still an important and quality-determining step for the advancement of SSNBs. Among the state-of-the-art materials, NaSICON-type $Na_{3+x}Zr_{2-}Si_{2+x}P_{1-x}O_{12}$, discovered nearly 50 years ago [10,11], stands out as the most promising candidate for application in SSNBs, because of its very high ionic conductivity, chemical stability, and dendrite tolerance against Na metal [12–15]. Notably, $Na_{3.4}Zr_2Si_{2.4}P_{0.6}O_{12}$ (NZSP) exhibits the highest reported total conductivity (σ_{total}) among all NaSICONs materials with 5.2×10^{-3} S cm^{-1} at 25 °C [12], and an even more extraordinary bulk conductivity (σ_{bulk}) of 1.5×10^{-2} S cm^{-1} at the same temperature [12]. This indicates the dominance of grain-boundary resistance (R_{gb}) to the total resistance (R_{total}) of the polycrystalline NZSP.

In practical applications, most conducting ceramics are polycrystalline, with σ_{total} influenced by both R_{bulk} and R_{gb}, respectively. While R_{bulk} is often emphasized as an intrinsic property of the ceramic, R_{gb} is taken as a given fact due to its complex and complicated parameters like secondary phases in the ceramic, defects, voids, dislocations, and inadequate grain-to-grain contact. However, in the case of practical applications, R_{gb} is of same importance as R_{bulk} since polycrystalline materials are much more extensively applied in industry compared to single-crystalline materials. Especially in the case of NaSICON ceramics, modifying the grain boundaries becomes even more crucial in order to further enhance σ_{total}, as R_{gb} predominates R_{total} in the ceramic [12,13]. The reason for high R_{gb} of NZSP is related to a thermal expansion anisotropy, which indicates a difference of thermal expansion along different lattice parameter directions. The thermal expansion coefficient of rhombohedral NZSP in the *c*-axis direction (10.7×10^{-6} K^{-1}) of the lattice is significantly higher than that in the *a*-axis (3.5×10^{-6} K^{-1}) [12, 16]. This leads to anisotropic contraction of the NZSP grains after sintering, resulting in insufficient compaction or even formation of micro-cracks between the grains, and thus a dominant R_{gb}. Until now, effective methods to eliminate or alleviate the impact of thermal expansion anisotropy for NaSICONs are unknown.

Additionally, NZSP has exhibited remarkable robustness against Na-metal dendrite formation. The critical current density (CCD) of Na | NZSP | Na symmetric cells reaches 14 mA cm^{-2} at room temperature (RT). and the cells can endure galvanostatic cycling at 1 mA cm^{-2}/1mAh cm^{-2} for 1000 h (at RT) [15], outperforming previously published metal | SE | metal symmetric cells. Nevertheless, it is well-established that defects within SEs, particularly at grain boundaries as well as electronic conductivity within grain boundaries, play a pivotal role in dendrite formation [15,17–21]. Thus, it is expected that eliminating or relieving the effect of TEA in NZSP could further improve its dendrite tolerance.

$Na_3LaP_2O_8$ (NLP) was reported as a side-product when La_2O_3 is added to the NaSICON-type $Na_3Zr_2Si_2PO_{12}$ with the aim to partially substitute Zr with La [22,23]. The purpose of these reports was to increase the σ_{bulk} of the NaSICON ceramics and they applied high La substitution level of >10 mol%. However, already in 1996, Miyajima et al. showed that cations with an ionic radius ≥0.92 Å have a very low solubility in $NaZr_2P_3O_{12}$ [24], while the ionic radius of La^{3+} is 1.03 Å. Although the resulting phase formation of NLP extracts Na and P from the NaSICON phase and make its stoichiometry rather undefined, the authors announced remarkable increases in σ_{bulk} and σ_{total} [22,23].

In our approach we therefore directly added NLP to the NaSICON phase to avoid a stoichiometric deterioration. Instead of the influence to σ_{bulk}, we observed a significant decrease in R_{gb} at the low level of NLP-modified NZSP resulting in an improved σ_{total}. An optimized amount of 2.5 mol% NLP shows the best performance (hereafter abbreviated as NZSP:NLP, details of the dependence of conductivity on NLP variation is given in Table S1). The dendrite tolerance of the NZSP:NLP is notably enhanced. The dendrite behavior of symmetric cells (Na | NZSP:NLP | Na) is also altered. The possible mechanism of the improvement is discussed.

2. Results and discussion

2.1. Ionic conductivities

In the present study, both the pristine NZSP and NZSP:NLP samples exhibit excellent density after sintering (relative density >95 %, both at sintering temperature of 1260 °C). Because of their similarity in sintering temperature and relative density, it can be concluded that NLP does not serve as a sintering aid for NZSP. The NZSP:NLP samples primarily display NaSICON phase, with small amounts of NLP but still detectable (even only 2.5 mol% NLP is added), indicating the low solubility of La element in NZSP structure [24]. Furthermore, there are no noticeable differences in the XRD patterns between the main phase of NZSP and NZSP:NLP samples (Fig. S1).

Fig. 1a presents the Nyquist plots of NZSP and NZSP:NLP, with the data of NZSP derived from a former publication [12]. To facilitate a direct comparison among the different samples, the impedances were calculated with the geometric sizes of the pellets. In NaSICON-type materials, it is common that only one semi-circle or even half of it appears in the impedance spectra at RT due to the limited frequency range (up to 10 MHz) of typical impedance spectroscopy systems [12,25]. Therefore, precisely distinguishing the contributions of R_{bulk} and R_{gb} becomes challenging. In this study, two impedance spectroscopy systems were employed in combination to overcome this issue, covering a high frequency (HF) range from 3 GHz to 1 MHz and a normal frequency (NF) range from 3 MHz to 1 Hz. As depicted in Fig. 1a, the Nyquist plot of both NZSP and NZSP:NLP shows two complete semi-circles. The impedance spectra can easily be fitted with the equivalent circuit given in Fig. 1a. Here L0, R and CPE indicate the inductance, resistance and constant phase element (CPE), respectively. The key parameters of the equivalent circuits are shown in Table 1. Given that the capacitance values of CPE1, CPE2 and CPE0 match well with the characteristic capacitance from the contribution of bulk (high-frequency semi-cycle), grain-boundary (middle-frequency semi-cycle) and the interface between electrolyte and electrodes (low-frequency line), respectively [26], R1 and R2 are attributed to R_{bulk} and R_{gb}, respectively.

For NZSP, R_{gb} is nearly twice as high as R_{bulk}, resulting in a much lower σ_{total} (5.2×10^{-3} S cm^{-1}, 25 °C) compared to σ_{bulk} (1.5×10^{-2} S cm^{-1}, 25 °C). This difference is actually already much better than what is typically seen in published impedance spectra of NaSICONs. In many cases, the σ_{total} can be orders of magnitude smaller than the σ_{bulk} for NaSICON materials [13]. The significant difference between R_{bulk} and R_{gb} in NaSICONs is primarily attributed to insufficient density after sintering and micro-cracking due to the thermal expansion anisotropy [12,22].

In the case of NZSP:NLP, R_{bulk} remains nearly constant (1.3×10^{-2} S cm^{-1}), but a significant decrease of R_{gb} is observed (Fig. 1a–Table 1), resulting in a much higher σ_{total} of 7.1×10^{-3} S cm^{-1}, even though NLP itself is an insulator, with the σ_{total} in the range of ~10^{-12} S cm^{-1} at RT [22]. It should be noted that both pristine and NLP modified samples in Fig. 1a have the same relative density of 97 %. Li et al. reported that adding La_2O_3 into NaSICON ceramic could result in NLP formation and higher σ_{total} [27]. However, the better performance came from the increased relative density of the NaSICON ceramic. La_2O_3 acted as a sintering aid in that study. In the present study, apparently it is not the case. Moreover, electronic conductivity of NZSP and NZSP:NLP was investigated (Fig. S2). At RT, pristine NZSP has an electronic conductivity of 1.9×10^{-9} S cm^{-1}, while NZSP:NLP shows an electronic conductivity of 8.3×10^{-10} S cm^{-1}. Both values are extremely low and favor the Coulombic efficiency and dendrite prevention during cycling of SSNBs [17,19]. In addition, both materials exhibit a wide electrochemical stability window up to 8V (Fig. S3) indicating the added NLP is redox stable in the tested voltage range. It is generally agreed that SEs possess better electrochemical stability window compared to liquid-based electrolytes (lower than 5 V) [13]. NaSICON-type SEs are especially outstanding in this aspect [12].

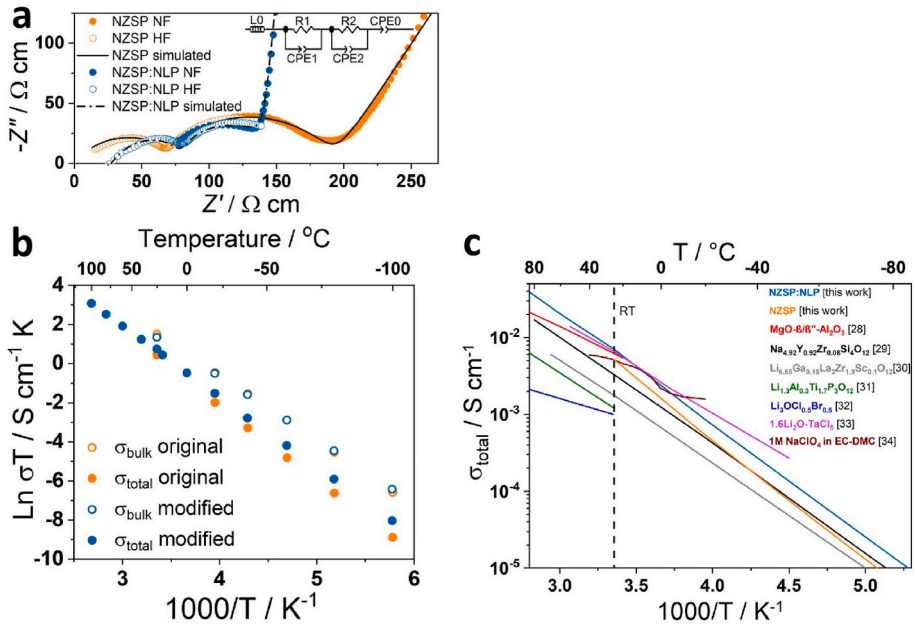

Fig. 1. a) Nyquist plot of the impedance spectra recorded at 25 °C with gold electrodes using a high-frequency (HF) analyzer (open symbols) and a normal-frequency (NF) analyzer (filled symbols) for NZSP (orange) and NZSP:NLP (blue) together with their fitted data (solid or dash line). Both samples have relative density of 97 %. b) Arrhenius plot of σ_{total} (filled symbols) and σ_{bulk} (open symbols) of NZSP (orange) and NZSP:NLP (blue). c) Temperature dependence of σ_{total} of NZSP and NZSP:NLP in comparison with other polycrystalline fast ion conductors. An amorphous oxide and a standard liquid electrolyte are also shown. (For interpretation of the references to color in this figure legend, the reader is referred to the Web version of this article.)

Table 1
Key parameters of the fitted equivalent circuit of NZSP samples shown in Fig. 1.

	R1 (Ω cm)	R2 (Ω cm)	CPE1 (F cm^{-1})	CPE2 (F cm^{-1})	CPE0 (F cm^{-1})
NZSP	67.2	124.8	4.5×10^{-12}	8.2×10^{-10}	3.0×10^{-6}
NZSP:NLP	77.9	62	4.2×10^{-12}	7.5×10^{-10}	8.5×10^{-7}

An Arrhenius plot of σ_{bulk} and σ_{total} for NZSP and NZSP:NLP is presented in Fig. 1b. All data follow ideal linear behavior. The σ_{bulk} values of NZSP and NZSP:NLP are very similar in the measured temperature range, indicating that NLP has a negligible influence on the crystal lattice of NZSP. However, the σ_{total} of NZSP:NLP is notably higher than that of NZSP, especially at low temperatures, highlighting the influence of NLP on the grain boundaries of NZSP. This property improvement also affects the activation energy. For σ_{bulk}, the same activation energy of 0.28 eV is determined. In contrast, the activation energy for σ_{total} has a difference of 0.02 eV (0.32 eV for NZSP, 0.30 eV for NZSP:NLP).

The obtained σ_{total} in this study is compared with other outstanding polycrystalline oxide-based fast ion-conducting SEs in Fig. 1c [28–32]. An amorphous oxide and a typical liquid electrolyte for Na-ion batteries are also included for comparison [33,34]. Many other SEs for Li or Na batteries show higher σ_{total} values compared to polycrystalline oxides, such as single-crystalline β/β”-alumina (>0.1 S cm^{-1} at RT) [35], sulfides like $Na_{2.88}Sb_{0.88}W_{0.12}S_4$ and $Li_{9.54}Si_{1.74}P_{1.44}S_{11.7}Cl_{0.3}$ (0.032 S cm^{-1} and 0.025 S cm^{-1} at RT, respectively) [36,37], or closo-boranes like $Na_2(CB_9H_{10})(CB_{11}H_{12})$ (0.06 S cm^{-1} at RT) [38]. However, considering cost-effectiveness, chemical and physical stability required for practical applications, polycrystalline oxides also demonstrate their irreplaceable excellence. Apart from NZSP discussed in this study, also other polycrystalline oxides have an ionic conductivity >1.0×10^{-3} S cm^{-1} at RT, which is widely regarded as the required level of σ_{total} for battery application. Polycrystalline β/β”-alumina represents another state-of-the-art SE for SSNBs, with a σ_{total} reaching 6.0×10^{-3} S cm^{-1} at RT [28]. $Na_5YSi_4O_{12}$-type SEs are also promising due to their low cost and high stability. Among them, $Na_{4.92}Y_{0.92}Zr_{0.08}Si_4O_{12}$ shows the best σ_{total} with 3.3×10^{-3} S cm^{-1} at RT [29]. In general, polycrystalline oxide Li-ion conductors tend to exhibit lower σ_{total} values compared to Na-ion conductors. The state-of-the-art $Li_7La_3Zr_2O_{12}$ and $Li_{1+x}Ti_{2-x}Al_xP_3O_{12}$ Li-ion conductors have prime σ_{total} values ranging from 1 to 2 $\times 10^{-3}$ S cm^{-1} at RT [30,31]. A relatively new group of materials are oxyhalogenides (Li_3OX with X = halogen element) which can reach 1.0 $\times 10^{-3}$ S cm^{-1} at RT [32]. It is worth to note that very recently, amorphous oxychlorides like $1.6Li_2O$-$TaCl_5$ have been reported to show high conductivities up to 6.6×10^{-3} S cm^{-1} at RT [33]. Traditionally, amorphous materials were considered to have insufficient σ_{total}, making this report a groundbreaking development in the field. Among all the aforementioned SEs in Fig. 1c, the NZSP:NLP stands out with an impressive σ_{total} of 7.1×10^{-3} S cm^{-1} at RT. This value even surpasses that of the commonly used liquid electrolyte, 1 M $NaClO_4$ in the mixture of ethylene carbonate and dimethyl carbonate (EC-DMC) [34], indicating a promising prospective of the NaSICON material.

2.2. Galvanostatic cycling

The improved σ_{total} also results in improve dendrite tolerance against Na metal, which can be verified from galvanostatic cycling tests with Na | NZSP | Na symmetric cells. Recently, it was observed that sodium dendrite growth occurred along the surface of NZSP rather than through the ceramic SE during the galvanostatic cycling of Na | NZSP | Na symmetric cells. The prevention of this phenomenon was confirmed by employing $NaNO_3$ as a surface protection [15]. In the current study, the same protective approach was applied for all electrochemical performance tests of Na | NZSP:NLP | Na symmetric cells. The symmetric cells were simply assembled by sticking Na electrodes onto the NZSP:NLP ceramic. No surface or interface modification was applied. Furthermore, it is widely recognized that strong polarizations occur between Na metal and SEs during the cycling of SSNBs and their lithium counterparts, because there might be a mismatch between the flux of ions (J_{ion}) across the metal | SE interface and the flux originating from metal self-diffusion ($J_{diffusion}$), leading to the formation of voids within the metal layer near

the interface and a decrease of contact area between the metal and the SE [14,15,17]. The process can be described with **Equation (1)**:

$$I_D = \frac{1}{2}\varphi F(\pi D)^{0.5} t_{max}^{-0.5} \quad (1)$$

where φ is the concentration of metal atoms in the anode, F is the Faraday constant, D is the self-diffusion coefficient of metal atoms in the metal. t_{max} indicates the theoretical upper limit of the operation time for a galvanostatic charge (discharge) under a specific current density (I_D) [14]. Once t_{max} is reached, the metal | SE interface will experience complete delamination. In order to mitigate these polarizations, external pressure is often applied to suppress the formation of voids. In this study, pressure was applied ranging from 6 to 24 MPa during the electrochemical performance tests of the symmetric cells shown in Fig. 2. The wide range of the pressure is due to the simplicity of the pressure-generation device of only tightened screws.

Fig. 2a illustrates the CCD test of a Na | NZSP:NLP | Na symmetric cell at an external pressure of ~6 MPa. With a cycling interval of 5 min per half cycle, the cycling curve remains stable within the range of ±2 to ±20 mA cm^{-2}. Observable short-circuit caused by dendrite formation happens at 22 mA cm^{-2}. Comparatively, the highest CCD value for Na | NZSP | Na symmetric cells is 14 mA cm^{-2} at RT at the same operation conditions [15]. When the cycling interval was increase to 30 min per half cycle, Na | NZSP:NLP | Na symmetric cell still show CCD value of 14 mA cm^{-2} at RT (Fig. S4). This indicates higher dendrite tolerance of NZSP:NLP ceramics compared to the pristine NZSP. Jaschin et al. reported superior CCD value up to 40 mA cm^{-2} between Na and NaSICON pellets, where they applied 3D structure of electrodes in both sides of the pellets and the actual contact area between metal and ceramic is much higher than the apparent area [39]. To the best of our knowledge, the CCD value of 22 mA cm^{-2} achieved in the present study is the highest reported value for Na-based symmetric cells with simple contact between Na and ceramics. In comparison, the CCD value of Li | SE based symmetric cells is generally almost one order of magnitude lower than this [17]. The important reasons are that the self-diffusion coefficient of Li is much lower than that of Na (5.1×10^{-11} *v.s.* 5.4×10^{-9} cm^2 s^{-1} at 25 °C, respectively, see **Equation (1)**) [14], as well as the superior conductivity and dendrite tolerance of NZSP:NLP.

Fig. 2b presents a long-term galvanostatic cycling test of a Na | NZSP:NLP | Na symmetric cell. In this test, a current density of ±2.0 mA cm^{-2} was applied to the cell for 1 h per half cycle, corresponding to an areal capacity of 2.0 mAh cm^{-2} per half cycle (equivalent to a thickness of 17.6 μm Na metal per charge or discharge). The test was conducted under pressure ranging from 6 to 12 MPa in a glovebox atmosphere, and at temperatures ranging from 21 to 26 °C. Before initiating the test, the impedance spectrum indicates a total resistance of the symmetric cell of 43 Ω at 23 °C. The voltage of the symmetric cells decreases during the initial cycles, because the initial contact area between the Na electrode and the pellet is smaller than the surface area of the NZSP:NLP pellet. It takes some time to optimize the contact between the Na electrode and the pellet under pressure, as well as during Na plating/stripping. After several hours, the voltage platform during galvanostatic cycling stabilizes, suggesting well-established contact between the Na electrodes and the pellet. At 97.6 h, the total resistance of the symmetric cell is 38 Ω at 23 °C (the impedance was tested when the galvanostatic cycling was paused; it is not an *operando* test). This corresponds to a σ_{total} of 6.6×10^{-3} S cm^{-1} when the resistance of the whole cell is regarded as R_{total} of the pellet, in good agreement with the σ_{total} of the NZSP:NLP tested with Au electrodes (Fig. 1a). The stable operation lasts for about 300 h. As the cycling progresses, the Na | NZSP:NLP interface begins to degrade, leading to observable polarization in each cycle, despite the continuous application of external pressure. After 650 h, the polarization accelerates from one side of the cell (Fig. S5). After 700 h, both sides reach the safety limitation of the testing system (8 V), significantly shortening the actual cycling time per half cycle. As polarization is commonly attributed to contact loss between Na and NZSP [14,15,17], a simplified calculation of this process is described with **Equation (2)**:

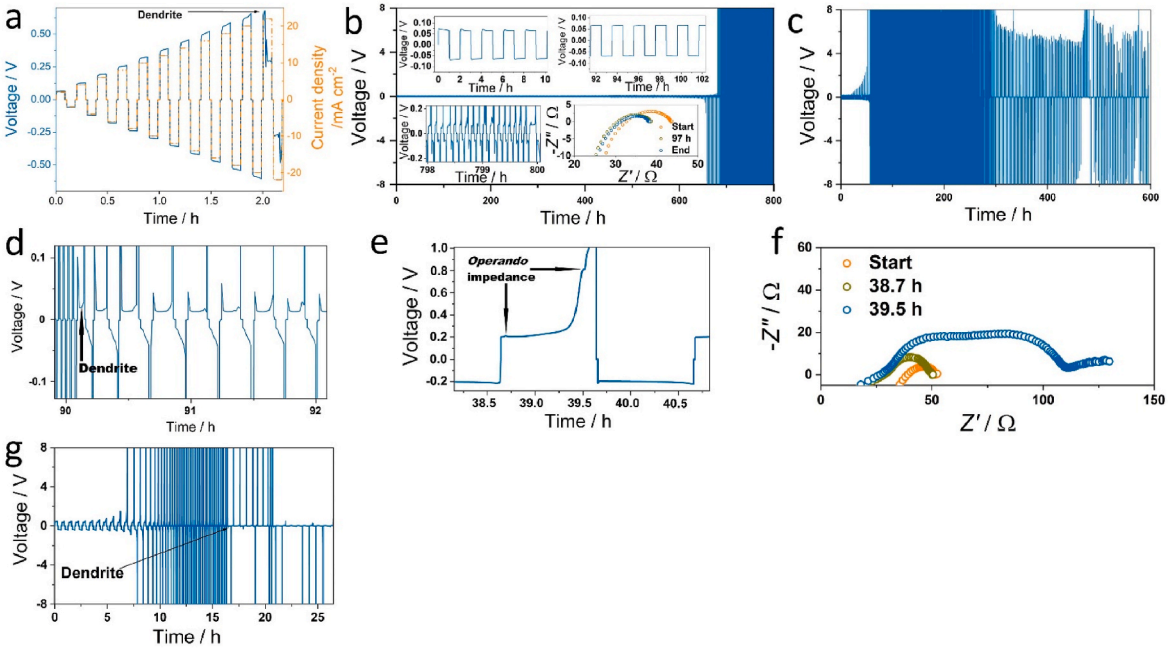

Fig. 2. a) CCD measurement on a Na|NZSP:NLP|Na symmetric cell at RT. The blue and the orange dashed line indicates the change in voltage and in current density, respectively. b) Galvanostatic cycling of a Na|NZSP:NLP|Na symmetric cell at 2.0 mA cm^{-2}, 2 mAh cm^{-2} (per half cycle) and RT. Enlarged partial views and Nyquist plot of the impedance spectra for the cell at different testing times are also shown as insets. c) Galvanostatic cycling of a Na|NZSP:NLP|Na symmetric cell at 5.0 mA cm^{-2}, 5 mAh cm^{-2} (per half cycle) and RT. d) Enlarged part of Fig. 2c to indicate the appearance of short-circuit caused by dendrite development. e) Partially enlarged plot of Fig. 2c to indicate the points in time for *operando* impedance measurements. f) *Operando* impedance spectra for the cell in Fig. 2c g) Galvanostatic cycling of a Na|NZSP:NLP|Na symmetric cell at 10.0 mA cm^{-2}, 2.5 mAh cm^{-2} (per half cycle) and RT. (For interpretation of the references to color in this figure legend, the reader is referred to the Web version of this article.)

$$V = \frac{d}{\sigma_{total} A} I \quad (2)$$

where V represents the voltage of the symmetric cell, I is the current applied in the test, σ_{total} is the conductivity of the NZSP:NLP, d is the thickness of the NZSP:NLP pellet, and A is the effective contact area between Na electrode and NZSP:NLP pellet. σ_{total} and d remain constant in the equation. At the beginning of the test, A is also a constant, equating to the surface area of the pellet because the Na electrodes are in good contact with the pellet. The set current density of I / A (here A is set as the surface area of the pellet) in the first 300 h generally aligns well with the actual local current density within the pellet, with stable V value of about 0.07 V. At 700 h, the value of V increased to 8 V because of the polarization. This signifies that the actual A at this point is more than 100 times smaller than the pellet's surface area, resulting in an actual instantaneous local current density of about 230 mA cm^{-2} at the interface where the Na electrode is still in contact with the pellet. In previous publications, obtaining such high data was only feasible through microscopic *in situ* scanning electron microscopy (SEM) microelectrode experiments within chemically clean areas and with dimensions of several tens of micrometers [15,17]. It is never shown in the realm of macroscopic samples. Near the end of the test, each charge or discharge period only takes 1–2 min to reach the limitation of 8 V. The small voltage platform still matches the value observed at about 90–100 h (Fig. 2b), indicating the absence of dendrites. This is further corroborated by the impedance spectrum analysis of the cell after 800 h of testing, where the impedance is almost the same as at 97.6 h, with a total cell resistance of 38 Ω. This also indicates that even though the contact between the Na electrode and NZSP:NLP can be severely compromised under DC current, and this critical state persists for over 100 h, the contact can be completely restored once the current is discontinued. In comparison, an increase of interface resistance of 1.5 Ω cm^2 was observed in a Na NZSP | Na symmetric cell after 1000 h operation at 1.0 mA cm^{-2}, 1 mAh cm^{-2} (per half cycle). This suggests a possible reaction occurred between Na metal and NZSP [15]. However, in the present study, the interface resistance of the cell remains 0 in the impedance spectra (within the detection limit of the testing system). The total cell resistance remains relatively constant throughout the 800 h testing duration after stabilization, indicating the better chemical compatibility of Na/NZSP:NLP compared to that of Na/NZSP. It should also be mentioned that the cell was analyzed after the cycling test by XRD and SEM. Both showed no obvious change in comparison to the fresh sample, indicating the reliable long-term stability of NZSP:NLP (Fig. S6).

When the current density in the galvanostatic cycling is increased to ±5.0 mA cm^{-2} (1 h per half cycle, corresponding to a thickness of 44.0 μm of Na metal has been cycled per charge or discharge), at the same testing conditions as shown in Fig. 2b, the Na | NZSP:NLP | Na symmetric cell can sustain stable operation for about 10 h (Fig. 2c and Fig. S7). Subsequently, observable polarization emerges as the cycling progresses. After 20 h, the polarization begins to accelerate (Fig. S7), and at approximately 50 h, it reaches the safety limit of the testing system (8 V). The cell continues to function under such severe polarization for additional 40 h, until the of a short-circuit finally occurs attributed to the growth of dendrites (at about 90 h, where the small plateau of the voltage is decreased to about 0.02 V, Fig. 2d). The short-circuit is further confirmed by impedance spectroscopic investigations (Fig. S8). Comparatively, Na | NZSP | Na symmetric cell can only survive at the same operating conditions for about 12 h before the formation of dendrites [15], further proving the higher dendrite tolerance of NZSP:NLP ceramics compared to the pristine NZSP as in the CCD tests.

To investigate the impact of DC current on the Na | NZSP:NLP interface, *operando* impedance measurements are applied by an additional independent testing probe, concurrently with DC cycling. Disturbance of impedance testing on DC cycling can be observed through two minor fluctuations in the voltage curve at 38.7 and 39.5 h (Fig. 2e). In comparison to the state before initiating the cycling test, the resistance of the symmetric cell remains almost unchanged when no polarization occurs during cycling, e.g. at 38.7 h (52 and 50 Ω, respectively, as shown in Fig. 2f), and no interface resistance is observable in both impedance spectra. However, when polarization arises from the steady voltage platform of 0.2 V–0.8 V (at 39.5 h), the *operando* impedance measurement exhibits a resistance of 65 Ω for the NZSP:NLP pellet and 45 Ω as the interface resistance between Na and NZSP:NLP, resulting in a total resistance of 110 Ω for the entire cell (Fig. 2f). The appearance of interface resistance suggests that part of the Na | NZSP:NLP interface has deteriorated and transitioned from pure resistance to a capacity-afflicted process. The increased apparent resistance of NZSP:NLP (from 50 to 65 Ω) indicates that part of the interface between Na and NZSP:NLP has experienced delamination. Moreover, when the galvanostatic current and voltage of the cycling are used to determine the DC resistance of cell, they exhibit 50 Ω and 200 Ω at 38.7 and 39.5 h, respectively. DC resistance and AC resistance (via impedance spectroscopy) correlate well with each other at the stable region of the cycling (38.7 h). However, during the polarization stage at 39.5 h, a significant discrepancy is observed between DC resistance (200 Ω) and AC resistance (110 Ω). This suggests a considerable portion of interface area between Na and NZSP:NLP is effectively "in contact" under AC signal, whereas it is ineffectively "in contact" under the DC signal. This phenomenon can be attributed to a "constriction effect" of the interface in AC mode, where minor pores and voids at the interface can be considered as having a "constriction resistance" [40]. In contrast, with the DC signal, the relative area is regarded as more detached. This indicates the complexity of the contact status between Na and NZSP:NLP during polarizations.

Although a short-circuit results from dendrite growth is observed at 90 h (Fig. 2d), the formed pathway of electronic conduction is not stable. It fractures after a few minutes, followed by a substantial increase in polarization up to 8 V. This cyclic pattern persists for over 500 h. There is neither a fully established dendrite network nor a complete disruption of the dendrite pathway. Instead, they remain in a delicate equilibrium. However, the cycling profile gradually shift towards the development of dendrite pathways, as evidenced by the extended duration of the small voltage platform indicating short-circuiting in the cycles (Fig. 2c). The analysis of the impedance spectra further corroborates this observation. At 94 h, the short-circuited cell exhibits a pure resistance of 10 Ω, which subsequently decreases to 5 Ω after the entire 600 h of cycling (Fig. S8). The reason behind the alternating occurrence of polarization and dendrite formation could be explained with a scenario in which, after the initial formation of a short-circuit, the Na film near the dendrite position might continue to be consumed during stripping, thereby isolating the formed dendrite. Consequently, polarization can emerge once again, since the cell is no longer in a short-circuited state. Conversely, during plating, the Na film could be re-deposited near the dendrite position, leading to another round of short-circuiting. The specifics of this phenomenon are elaborated schematically in Fig. S9.

With a further increase in the current density to ±10.0 mA cm^{-2} (Fig. 2g, the external pressure is increased to 12–24 MPa), the electrochemical behavior remains similar to that as observed with ±5.0 mA cm^{-2}. However, the kinetics of all the individual stages are notably shorter: stable operation (3 h, Fig. S10), severe polarization leading to 8 V (7 h), short-circuit due to dendrite growth (16 h, Figure S10 and Figure S11), and the appearance of alternating short-circuit and polarization after 16 h are observed.

Similar behavior is even seen in some CCD tests of Na | NZSP:NLP | Na symmetric cells. An example is shown in Fig. S12. The voltage of the symmetric cell polarizes to 8 V when the current density is at 12 mA cm^{-2}, while the final short-circuit appears at 28 mA cm^{-2}. Even after short-circuiting, polarization up to 8 V still appears in the continuous cycling (Fig. S12a), indicating that the formed electronic conduction path is not stable and can be interrupted continuous cycling. Clearly, the cycling profile of short-circuit/polarization loop extensively exists in all kinds of galvanostatic cycling tests for Na | NZSP:NLP | Na symmetric

cells.

The present study represents the initial exploration of the failure mode resulting from the combination of polarization and dendrite formation, which is attributed to the exceptional dendrite tolerance demonstrated in this work, with apparent cycling current density reaching tens of mA cm^{-2} and actual local current density reaching 230 mA cm^{-2}. In contrast, prior reports documented dendrite formation before noticeable polarization. Nevertheless, it should be recognized that extreme polarization also constitutes a failure mode for the cells, rendering them unusable under such highly polarized voltage conditions. Table 2 gives a comparison of the galvanostatic cycling performance of the Na | NZSP | Na symmetric cells in this study with published outstanding results of metal | SE | metal cells, indicating the high quality of the findings presented here. It should be mentioned that in Table 2, the "failure" of the tested cells in this study indicates the polarization reaching 8 V, while for all other symmetric cells, it refers to the occurrence of short-circuits caused by dendrite growth. Evidently, NZSP:NLP also exhibits superior dendrite-tolerance compared to NZSP.

2.3. Microstructures

Unlike the discussion to the σ_{bulk}, which is primarily determined by the crystal structure and constituent elements and can be easily characterized by various techniques like XRD, neutron scattering, synchrotron X-ray etc., and even be easily simulated by machine learning [49–53], investigating the conductivity of the grain boundaries represents significant challenges. Grain boundaries contain defects, dislocations, imperfect grain-to-grain contacts, and secondary phases (both crystalline and amorphous), which complicate precise characterization. The possible mechanism of the enhanced σ_{total} and dendrite tolerance of NZSP:NLP compared to pristine NZSP ceramics can only be investigated by the characterization of their microstructures. Fig. 3a and **b** compare the microstructure of cross-sections of sintered NZSP and NZSP:NLP by scanning electron microscopy (SEM). In order to minimize the impact of mechanical forces to the ceramics, Ar-etching was employed to polish both cross-sections. As mentioned above, the influence of thermal expansion anisotropy is evident in the microstructural grain boundaries of the NZSP. Insufficient contact between grains and even the occurrence of cracks along the grain boundaries of the NZSP are clearly visible. In contrast, with the addition of NLP, the detachment of the grain boundaries is significantly mitigated. The contact between the grains of NZSP:NLP is much tighter, to the point where it becomes challenging to distinguish individual grains. This observation effectively explains the substantial difference in R_{gb} between the NZSP and NZSP:NLP as shown in Fig. 1. At the same time, it is generally regarded that the dendrite growth of the Li (Na) metal is frequently through the defects of the grain-boundaries or pores in SEs [15,17,18,54–56]. The reinforced microstructure of the grain-boundaries of NZSP:NLP is also beneficial for the dendrite tolerance.

NLP agglomerations can be observed in backscattered electron SEM images (Fig. 3b) as light gray particles. In addition, very few white particles can be seen in Fig. 3b. The bright color indicates particles with large atomic number, presumably La_2O_3. However, due to their small dimension and the decomposition of NZSP under the electron beam, a detailed elemental analysis is only reliable with high-angle annular dark-field (HAADF)-scanning transmission electron microscopy (STEM) in combination with energy dispersive X-ray spectroscopy (EDX) under cryogenic conditions (Fig. 4). The samples for STEM were prepared by focused ion beam (FIB) cutting. It should be noted that NaSICON is sensitive to charging during FIB, which leads to sodium displacement during TEM preparation at RT. Cryogenic preparation and the application of a protective conducting layer were employed to minimize damage to the NZSP samples [57,58]. The images of FIB-cut NZSP are presented in Fig. S13, further confirming the improved grain-to-grain contact in NZSP:NLP compared with NZSP.

Through EDX element mapping, areas with enrichment of Na, La and P elements are clearly discernible at which Si and Zr contents are also clearly reduced. The molar ratio of Na: La: P is approximately 3:1:2 within the detection accuracy of EDX element mapping, indicating the existence of NLP in the NZSP ceramic after sintering. The particle size of NLP phase is in the range of 0.1–1 μm, with an average size of about 0.5 μm. The presence of NLP detected in SEM and TEM, the very small but still observable NLP content in the XRD patterns (Fig. S1) without any shift of the reflections between NZSP and NZSP:NLP, suggest that the added NLP does not form a solid solution with the NaSICON main phase. All NLP particles are primarily concentrated at the grain boundaries of the ceramic, particularly at the junctions where multiple grains meet. The exact mechanism responsible for the formation of the NLP-phase morphology during sintering remains unknown yet, but the SEM images indicate a filling of the individual remaining pores (Fig. 3a) and inducing additional bonds between the two materials. It is likely that the similar chemical nature of both materials, i.e. the two open framework structures, facilitate strong bonds between $(Si,P)O_4^{3-}$ polyhedra at the interfaces. Further investigations are required to uncover the underlying

Table 2
Cycling performance of different metal | SE | metal symmetric cells tested at RT.

Metal | SE combination	Interface resistance (Ω cm^2)	Current density (mA cm^{-2})	Areal capacity per half cycle (mAh cm^{-2})	Total areal capacity before failure (mAh cm^{-2})	Time to failure (h)	Pressure applied (MPa)	Ref.
Na |β"-Al_2O_3	8	0.5–5.5	3.0	33	38	3.4	[41]
Li-W | $Li_{6.4}La_3Zr_{1.4}Ta_{0.6}O_{12}$	n.a.	0.4	0.03	86	215	0.16	[42]
Na | $Na_{3.2}Zr_{1.9}Ca_{0.1}Si_2PO_{12}$	175	0.1–0.3	0.1–0.3	150	600	n.a.	[43]
Li | Li_6PS_5Cl	n.a.	0.05 and 4	0.5	170	1720	0.1–7	[21]
Li | $Li_{6.4}La_3Zr_{1.4}Ta_{0.6}O_{12}$	7	2.2	0.88	176	80	5	[44]
Li−ZnF_2 | $Li_{6.4}La_3Zr_{1.4}Ta_{0.6}O_{12}$	11.3	0.4	0.4	540	1350	n.a.	[45]
Na | NZSP	1.7	1	5	550	570	0	[14]
Li | $Li_{6.5}La_3Zr_{1.5}Ta_{0.5}O_{12}$ with $AgNO_3$ interlayer	4.5	0.2	0.1	700	3500	n.a.	[46]
Li-Ag | LiI- Li_6PS_5Cl	n.a.	0.5	0.5	800	1600	n.a.	[47]
$Na_3Zr_2Si_2PO_{12}$ deposited with Graphene	46	1	1	1000	1000	n.a.	[48]
Na | NZSP	0	5	5	60	12	6–12	[15]
Na | NZSP	0	3	3	531	180	6–12	[15]
Na | NZSP	0–1.5	1	1	1000	1030	6–12	[15]
Na | NZSP:NLP	0	10	2.5	50	16	12–24	This work
Na | NZSP:NLP	0	5	5	255	90	6–12	This work
Na | NZSP:NLP	0	2	2	1300	800	6–12	This work

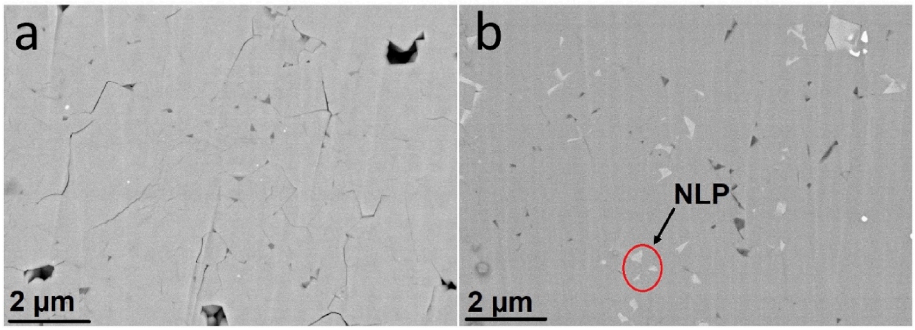

Fig. 3. SEM images of a polished cross-section area of a) NZSP and b) NZSP:NLP.

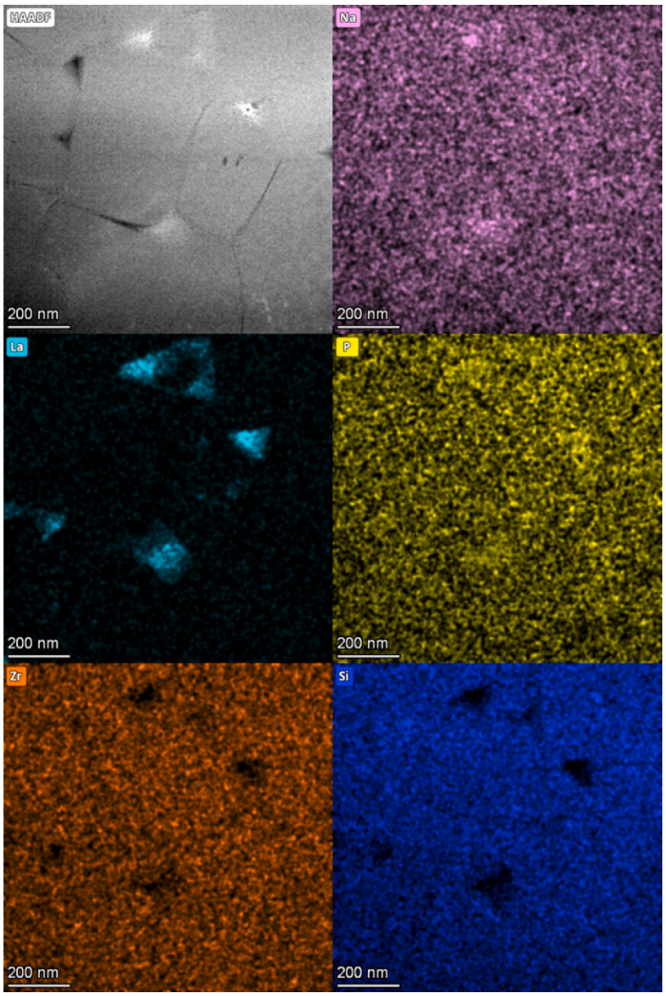

Fig. 4. HAADF-STEM image and EDX element maps of FIB-cut TEM lamellas of NZSP:NLP.

principles. Nevertheless, it is reasonable to conclude that NLP acts as a reinforcing agent within the ceramic, effectively binding the NZSP grains together at their grain boundaries.

It should be noted that, although the NZSP:NLP exhibits lower R_{gb} and consequently higher σ_{total} compared to NZSP, their thermal expansion anisotropy is very similar. The difference in thermal expansion coefficient between the *a*-axis and *c*-axis of the NZSP:NLP is $3.6 \times 10^{-6}\,K^{-1}$ *vs.* $10.6 \times 10^{-6}\,K^{-1}$, respectively (Fig. S14), which is very close to the values of pristine NZSP ($3.5 \times 10^{-6}\,K^{-1}$ *vs.* $10.7 \times 10^{-6}\,K^{-1}$, respectively). This indicates that the modification of NLP doesn't alter the thermal expansion anisotropy. The small changes in the lattice parameters are related to small changes in the NaSICON stoichiometry (formation of La_2O_3 or other Na-La compounds). The observation is also consistent with the fact that the NZSP:NLP shows no noticeable differences in crystal structure compared to the pristine NZSP (Fig. S1). There must be another mechanism that counteracts the effect of thermal expansion anisotropy in the NZSP:NLP, resulting in the lower R_{gb} of the samples. However, further investigations are still required to fully elucidate this mechanism.

3. Conclusions

NZSP ceramics are modified with 2.5 mol% NLP. On one hand, NLP does not serve as a sintering aid for NZSP because the sintering temperature and relative density of NZSP is not changed. On the other hand, although the added NLP does not alter the thermal expansion anisotropy of NZSP, it optimizes the microstructure of the grain boundaries by mitigating the micro-crack formation and reinforcing the inter-grain contact. Therefore, NZSP:NLP exhibits significantly lower R_{gb} in comparison to the pristine material, leading to an exceptional σ_{total} of 7.1×10^{-3} S cm^{-1} at 25 °C, outclassing other oxidic polycrystalline SEs. Simultaneously, the electronic conductivity of NZSP:NLP is also reduced to 8.3×10^{-10} S cm^{-1} at RT. Both pristine and modified NZSP have a wide electrochemical stability window up to 8 V. The reinforced grain-boundary microstructure and diminished electronic conductivity results in an extraordinary level of dendrite tolerance in the Na | NZSP:NLP | Na symmetric cells. The CCD of Na | NZSP:NLP | Na symmetric cells is increased to 22 mA cm^{-2}. The galvanostatic cycling of the cells under 2 mA cm^{-2}/2 mAh cm^{-2}, 5 mA cm^{-2}/5 mAh cm^{-2} and 10 mA cm^{-2}/2.5 mAh cm^{-2} (all for half cycle) are demonstrated for 800 h, 90 h, and 16 h, respectively. The failure mode of the cells shifts from typical dendrite formation to the loop of substantial polarizations and short-circuits.

4. Experimental

NZSP and NZSP:NLP powder was synthesized using a solution-assisted solid-state reaction method [12,25]. $NaNO_3$ (VWR), $ZrO(NO_3)_2$ (Aldrich), $Si(OCH_2CH_3)_4$ (Merck), $NH_4H_2PO_4$ (Merck) and $La(NO_3)_3{\cdot}6H_2O$ (Aldrich) were used as starting materials. All the chemicals applied in this study were analytically pure. As a specific example for the preparation of 0.025 mol NZSP, first $ZrO(NO_3)_2$ was dissolved in deionized water to form a Zr solution, and the concentration of Zr in the solution was determined by thermogravimetry. This is because $ZrO(NO_3)_2$ can not be accurately weighted because of its water absorbing nature. In the example case, the mass fraction of Zr (expressed by the amount of ZrO_2) in the solution was 11.75 wt%. 7.224g $NaNO_3$ was dissolved in deionized water and 52.43 g Zr solution was added. 12.500g $Si(OCH_2CH_3)_4$ was also added to the solution while stirring together with 5 ml 65 % HNO_3 (Aldrich). When the $Si(OCH_2CH_3)_4$ was hydrolyzed, 1.725g $NH_4H_2PO_4$ was added to the system during stirring. The homogeneous aqueous solution immediately showed precipitation of complex zirconium oxyphosphate compounds. The whole mixture was

dried at 85 °C. The dried powder was then calcined at 800 °C for 3 h. After calcination, a white powder was obtained. The calcined powder was then milled in 96 % ethanol with zirconia balls on a milling bench for 48 h, and dried at 70 °C for 12 h. With this drying step the processing of the NZSP raw powder was then finished. The preparation of 0.025 mol NZSP:NLP is the same like that of NZSP, but with extra 0.159g $NaNO_3$, 0.271g $La(NO_3)_3{\cdot}6H_2O$ and 0.144g $NH_4H_2PO_4$ in the precursor solution of NZSP. And the final powder was ball-milled with pure ethanol once again.

The powders were put into a cylindrical pressing mold (8 mm or 13 mm in diameter) and pressed with a uniaxial pressure of about 100 MPa at room temperature. The pressed pellets were sintered at 1260 °C for 5 h. The obtained pellets had a thickness of 1–3 mm. The relative density of the sintered pellets was >95 %. For conductivity tests, a sputter coater (Ted Pella Inc., Cressington 108 auto) was used to prepare Au | SE | Au symmetric cells. The temperature-dependent impedance spectra were recorded between 373 K and 173 K in a temperature-controlled chamber (Novocontrol Technologies BDS1100). Two commercial electrochemical systems (Keysight E4991B and Novocontrol Technologies Alpha-A) with an AC frequency range from 3 GHz to 1 MHz and from 3 MHz to 1 Hz were applied for impedance spectroscopy, respectively. An alternating voltage amplitude of 20 mV was used during measurements. The data analysis and fitting of the impedance data for both frequency ranges were performed with the Z-view software (Scribner Associates Inc.).

For the NZSP:NLP samples with Na electrodes, a surface protection was applied first. A small paintbrush was dipped into a saturated solution of sodium salt (such like $NaNO_3$), and then the solution was carefully brushed onto the outer surface of the pellets where it is not supposed to be covered by Na metal electrodes. The wet coating was dried in vacuum at 70 °C for 10 min. The above painting process was repeated for 3–5 times to achieve complete surface coverage. Na metal sheets were attached directly onto the surfaces of the pellets by mechanical pressing with the force of about 1 kN (~12 MPa). The thickness of the metal electrode was 0.2–1 mm. A homemade testing bench with two metal plates and screws was used to press the symmetric cells during electrochemical testing. The pressure was generated by tightening the screws and measured by a force sensor (GM 77, Lorenz Messtechnik GmbH). Electrochemical tests were carried out inside a glovebox monitoring the oxygen content (GS Glovebox Systemtechnik GmbH). Impedance spectra of the Na | NZSP:NLP | Na symmetric cells were measured using a commercial electrochemical system (BioLogic VMP-300) with an AC frequency range from 3 MHz to 1 Hz, and fitted with the software Z-view. The current-voltage behavior of the cells was tested using the same electrochemical system.

The crystal structure of the ceramics was characterized by XRD using a Bruker D4 Endeavor diffractometer with Cu K_α radiation. The microstructure of the ceramics was investigated by field-emission SEM (ZEISS Merlin) on the cross section of the pellets polished by an Ar cross-section polisher (JEOL, SM-09010). To further characterize the grain boundaries of the samples, cross-sections of the ceramics were prepared with a XEIA3 system (TESCAN GmbH). Samples were attached to a Leica stub with adhesive copper tape and transferred using the Leica EM VCT500 system (Leica Microsystems GmbH). Before milling, the samples were cooled to −133 °C by liquid nitrogen and cooling was maintained during the analysis. Xe^+ ions with an energy of 30 kV were used in all experiments. Beam currents for milling and polishing were set to 2 μA and 30 nA, respectively. For preparation of the electron-transparent specimens an Auriga 60 cross-beam system (Carl Zeiss NTS GmbH) with a liquid nitrogen stage (GATAN GmbH; operation temperature: −185 °C) was used. Thinning process of the TEM lamella was performed using Ga^+ ions at 30 kV and a beam current of 240 pA. HAADF-STEM analysis was performed using an aberration-corrected Themis 300 system (Thermo Fischer Scientific) using a beam energy of 300 kV and a nominal screen current of 70 pA. EDX analysis was conducted with a Super-X EDX detector. Characterization was carried out under cryogenic conditions (−185 °C) using a liquid nitrogen-cooled 915 cryo transfer holder (GATAN GmbH). Data evaluation was conducted using Velox software package (Thermo Fischer Scientific).

CRediT authorship contribution statement

Limin Liu: Writing – original draft, Methodology, Investigation. **Qianli Ma:** Writing – original draft, Supervision, Methodology, Investigation, Conceptualization. **Xiaoliang Zhou:** Writing – original draft, Supervision, Project administration, Funding acquisition, Conceptualization. **Ziming Ding:** Writing – review & editing, Methodology, Investigation. **Daniel Grüner:** Writing – review & editing, Methodology, Investigation. **Christian Kübel:** Writing – review & editing, Supervision. **Frank Tietz:** Writing – review & editing, Supervision, Conceptualization.

Declaration of competing interest

The authors declare that they have no known competing financial interests or personal relationships that could have appeared to influence the work reported in this paper.

Acknowledgements

The authors thank Dr. Yoo-Jung Sohn from IMD for high temperature XRD investigations. L.L. and X.Z. thank the National Key R&D Program of China (2021YFB4001502), National Natural Science Foundation of China (No. 22075231), and the Sichuan Science and Technology Program (No. 2021YFSY0022) for financial support. Z.D. and C.K. thank the German Research Foundation (DFG) under Project ID 390874152 (POLiS Cluster of Excellence). This work contributes to the research performed at CELEST (Center for Electrochemical Energy Storage Ulm-Karlsruhe).

Appendix A. Supplementary data

Supplementary data to this article can be found online at https://doi.org/10.1016/j.jpowsour.2024.235773.

Data availability

Data will be made available on request. TEM data is open at: https://radar.kit.edu/radar/en/dataset/1n8u3z4zvh9w76ch

References

[1] D. Larcher, J.-M. Tarascon, Towards greener and more sustainable batteries for electrical energy storage, Nat. Chem. 7 (2015) 19–29.
[2] X. Xiang, K. Zhang, J. Chen, Recent advances and prospects of cathode materials for sodium-ion batteries, Adv. Mater. 27 (2015) 5343–5364.
[3] S. Chen, C. Wu, L. Shen, C. Zhu, Y. Huang, K. Xi, J. Maier, Y. Yu, Challenges and perspectives for NASICON-type electrode materials for advanced sodium-ion batteries, Adv. Mater. 29 (2017) 1700431.
[4] P.K. Nayak, L. Yang, W. Brehm, P. Adelhelm, From lithium-ion to sodium-ion batteries: advantages, challenges, and surprises, Angew. Chem. Int. Ed. 57 (2018) 102–120.
[5] J. Janek, W.G. Zeier, A solid future for battery development, Nat. Energy 1 (2016) 1–4.
[6] C. Zhao, L. Liu, X. Qi, Y. Lu, F. Wu, J. Zhao, Y. Yu, Y.S. Hu, L. Chen, Solid-state sodium batteries, Adv. Energy Mater. 8 (2018) 1703012.
[7] J.F. Wu, R. Zhang, Q.F. Fu, J.S. Zhang, X.Y. Zhou, P. Gao, C.H. Xu, J. Liu, X. Guo, Inorganic solid electrolytes for all-solid-state sodium batteries: fundamentals and strategies for battery optimization, Adv. Funct. Mater. 31 (2021) 2008165.
[8] Y. Guo, S. Wu, Y.-B. He, F. Kang, L. Chen, H. Li, Q.-H. Yang, Solid-state lithium batteries: safety and prospects, eScience 2 (2022) 138–163.
[9] Y. Wang, Z. Wang, D. Wu, Q. Niu, P. Lu, T. Ma, Y. Su, L. Chen, H. Li, F. Wu, Stable Ni-rich layered oxide cathode for sulfide-based all-solid-state lithium battery, eScience 2 (2022) 537–545.
[10] H.-P. Hong, Crystal structures and crystal chemistry in the system $Na_{1+x}Zr_2Si_xP_{3-x}O_{12}$, Mater. Res. Bull. 11 (1976) 173–182.
[11] J.B. Goodenough, H.-P. Hong, J. Kafalas, Fast Na^+-ion transport in skeleton structures, Mater. Res. Bull. 11 (1976) 203–220.

[12] Q. Ma, C.-L. Tsai, X.-K. Wei, M. Heggen, F. Tietz, J.T. Irvine, Room temperature demonstration of a sodium superionic conductor with grain conductivity in excess of 0.01 S cm^{-1} and its primary applications in symmetric battery cells, J. Mater. Chem. A 7 (2019) 7766–7776.

[13] Q. Ma, F. Tietz, Solid-state electrolyte materials for sodium batteries: towards practical applications, Chemelectrochem 7 (2020) 2693–2713.

[14] C.-L. Tsai, T. Lan, C. Dellen, Y. Ling, Q. Ma, D. Fattakhova-Rohlfing, O. Guillon, F. Tietz, Dendrite-tolerant all-solid-state sodium batteries and an important mechanism of metal self-diffusion, J. Power Sources 476 (2020) 228666.

[15] Q. Ma, T. Ortmann, A. Yang, D. Sebold, S. Burkhardt, M. Rohnke, F. Tietz, D. Fattakhova-Rohlfing, J. Janek, O. Guillon, Enhancing the dendrite tolerance of NaSICON electrolytes by suppressing edge growth of Na electrode along ceramic surface, Adv. Energy Mater. 12 (2022) 2201680.

[16] F. Tietz, Sodium-Ion Batteries: Materials, Characterization, and Technology, vol. 2, Wiley, editor .

[17] T. Krauskopf, F.H. Richter, W.G. Zeier, J. Janek, Physicochemical concepts of the lithium metal anode in solid-state batteries, Chem. Rev. 120 (2020) 7745–7794.

[18] H. Wang, H. Gao, X. Chen, J. Zhu, W. Li, Z. Gong, Y. Li, M.S. Wang, Y. Yang, Linking the defects to the formation and growth of Li dendrite in all-solid-state batteries, Adv. Energy Mater. 11 (2021) 2102148.

[19] X. Liu, R. Garcia-Mendez, A.R. Lupini, Y. Cheng, Z.D. Hood, F. Han, A. Sharafi, J. C. Idrobo, N.J. Dudney, C. Wang, Local electronic structure variation resulting in Li 'filament' formation within solid electrolytes, Nat. Mater. 20 (2021) 1485–1490.

[20] Y. Liu, X. Xu, X. Jiao, O.O. Kapitanova, Z. Song, S. Xiong, Role of interfacial defect on electro-chemo-mechanical failure of solid-state electrolyte, Adv. Mater. (2023) 2301152.

[21] Z. Ning, G. Li, D.L. Melvin, Y. Chen, J. Bu, D. Spencer-Jolly, J. Liu, B. Hu, X. Gao, J. Perera, Dendrite initiation and propagation in lithium metal solid-state batteries, Nature 618 (2023) 287–293.

[22] Z. Zhang, Q. Zhang, J. Shi, Y.S. Chu, X. Yu, K. Xu, M. Ge, H. Yan, W. Li, L. Gu, A self-forming composite electrolyte for solid-state sodium battery with ultralong cycle life, Adv. Energy Mater. 7 (2017) 1601196.

[23] F. Sun, Y. Xiang, Q. Sun, G. Zhong, M.N. Banis, W. Li, Y. Liu, J. Luo, R. Li, R. Fu, Insight into ion diffusion dynamics/mechanisms and electronic structure of highly conductive sodium-rich $Na_{3+x}La_xZr_{2-x}Si_2PO_{12}$ ($0 \leq x \leq 0.5$) solid-state electrolytes, ACS Appl. Mater. Interfaces 13 (2021) 13132–13138.

[24] Y. Miyajima, Y. Saito, M. Matsuoka, Y. Yamamoto, Ionic conductivity of NASICON-type $Na_{1+x}M_xZr_{2-x}P_3O_{12}$ (M: Yb, Er, Dy), Solid State Ionics 84 (1996) 61–64.

[25] Q. Ma, M. Guin, S. Naqash, C.-L. Tsai, F. Tietz, O. Guillon, Scandium-substituted $Na_3Zr_2(SiO_4)_2(PO_4)$ prepared by a solution-assisted solid-state reaction method as sodium-ion conductors, Chem. Mater. 28 (2016) 4821–4828.

[26] J.T. Irvine, D.C. Sinclair, A.R. West, Electroceramics: characterization by impedance spectroscopy, Adv. Mater. 2 (1990) 132–138.

[27] W. Li, N. Zhao, Z. Bi, X. Guo, Insight into synergetic effect of bulk doping and boundary engineering on conductivity of NASICON electrolytes for solid-state Na batteries, Appl. Phys. Lett. 121 (2022) 033901.

[28] G. May, A. Hooper, The effect of microstructure and phase composition on the ionic conductivity of magnesium-doped sodium-beta-alumina, J. Mater. Sci. 13 (1978) 1480–1486.

[29] A. Yang, Enhanced room-temperature Na^+ ionic conductivity in $Na_{4.92}Y_{0.92}Zr_{0.08}Si_4O_{12}$, eScience 3 (2023) 100175.

[30] L. Buannic, B. Orayech, J.-M. Lopez Del Amo, J. Carrasco, N.A. Katcho, F. Aguesse, W. Manalastas, W. Zhang, J. Kilner, A. Llordés, Dual substitution strategy to enhance Li^+ ionic conductivity in $Li_7La_3Zr_2O_{12}$ solid electrolyte, Chem. Mater. 29 (2017) 1769–1778.

[31] F. Ma, E. Zhao, S. Zhu, W. Yan, D. Sun, Y. Jin, C. Nan, Preparation and evaluation of high lithium ion conductivity $Li_{1.3}Al_{0.3}Ti_{1.7}(PO_4)_3$ solid electrolyte obtained using a new solution method, Solid State Ionics 295 (2016) 7–12.

[32] Y. Zhao, L.L. Daemen, Superionic conductivity in lithium-rich anti-perovskites, J. Am. Chem. Soc. 134 (2012) 15042–15047.

[33] S. Zhang, F. Zhao, J. Chen, J. Fu, J. Luo, S.H. Alahakoon, L.-Y. Chang, R. Feng, M. Shakouri, J. Liang, Y. Zhao, X. Li, L. He, Y. Huang, T.-K. Sham, X. Sun, A family of oxychloride amorphous solid electrolytes for long-cycling all-solid-state lithium batteries, Nat. Commun. 14 (2023) 3780.

[34] A. Bhide, J. Hofmann, A.K. Dürr, J. Janek, P. Adelhelm, Electrochemical stability of non-aqueous electrolytes for sodium-ion batteries and their compatibility with $Na_{0.7}CoO_2$, Phys. Chem. Chem. Phys. 16 (2014) 1987–1998.

[35] J. Briant, G. Farrington, Ionic conductivity in Na^+, K^+, and Ag^+ β″-alumina, J. Solid State Chem. 33 (1980) 385–390.

[36] A. Hayashi, N. Masuzawa, S. Yubuchi, F. Tsuji, C. Hotehama, A. Sakuda, M. Tatsumisago, A sodium-ion sulfide solid electrolyte with unprecedented conductivity at room temperature, Nat. Commun. 10 (2019) 5266.

[37] Y. Kato, S. Hori, T. Saito, K. Suzuki, M. Hirayama, A. Mitsui, M. Yonemura, H. Iba, R. Kanno, High-power all-solid-state batteries using sulfide superionic conductors, Nat. Energy 1 (2016) 1–7.

[38] W.S. Tang, K. Yoshida, A.V. Soloninin, R.V. Skoryunov, O.A. Babanova, A. V. Skripov, M. Dimitrievska, V. Stavila, S.-i. Orimo, T.J. Udovic, Stabilizing superionic-conducting structures via mixed-anion solid solutions of monocarba-closo-borate salts, ACS Energy Lett. 1 (2016) 659–664.

[39] P.W. Jaschin, C.R. Tang, E.D. Wachsman, High-rate cycling in 3D dual-doped NASICON architectures toward room-temperature sodium-metal-anode solid-state batteries, Energy Environ. Sci. 17 (2024) 727–737.

[40] J.K. Eckhardt, P.J. Klar, J. Janek, C. Heiliger, Interplay of dynamic constriction and interface morphology between reversible metal anode and solid electrolyte in solid state batteries, ACS Appl. Mater. Interfaces 14 (2022) 35545–35554.

[41] M.C. Bay, M. Wang, R. Grissa, M.V. Heinz, J. Sakamoto, C. Battaglia, Sodium plating from Na-β″-alumina ceramics at room temperature, paving the way for fast-charging all-solid-state batteries, Adv. Energy Mater. 10 (2020) 1902899.

[42] V. Raj, V. Venturi, V.R. Kankanallu, B. Kuiri, V. Viswanathan, N.P.B. Aetukuri, Direct correlation between void formation and lithium dendrite growth in solid-state electrolytes with interlayers, Nat. Mater. 21 (2022) 1050–1056.

[43] Y. Lu, J.A. Alonso, Q. Yi, L. Lu, Z.L. Wang, C. Sun, A high-performance monolithic solid-state sodium battery with Ca^{2+} doped $Na_3Zr_2Si_2PO_{12}$ electrolyte, Adv. Energy Mater. 9 (2019) 1901205.

[44] H. Zheng, S. Wu, R. Tian, Z. Xu, H. Zhu, H. Duan, H. Liu, Intrinsic lithiophilicity of Li–garnet electrolytes enabling high-rate lithium cycling, Adv. Funct. Mater. 30 (2020) 1906189.

[45] L. Zhang, Q. Meng, Y. Dai, X. Feng, M. Shen, Q. Zhuang, Z. Ju, R. Zheng, Z. Wang, Y. Cui, Ion/electron conductive layer with double-layer-like structure for dendrite-free solid-state lithium metal batteries, Nano Energy (2023) 108573.

[46] M. Cai, Y. Lu, J. Su, Y. Ruan, C. Chen, B.V. Chowdari, Z. Wen, In situ lithiophilic layer from H^+/Li^+ exchange on garnet surface for the stable lithium-solid electrolyte interface, ACS Appl. Mater. Interfaces 11 (2019) 35030–35038.

[47] Y.-L. Liao, J.-K. Hu, Z.-H. Fu, C.-Z. Zhao, Y. Lu, S. Li, S.-J. Yang, S. Sun, X.-L. Wang, J. Liu, Integrated interface configuration by in-situ interface chemistry enabling uniform lithium deposition in all-solid-state lithium metal batteries, J. Energy Chem. 80 (2023) 458–465.

[48] E. Matios, H. Wang, C. Wang, X. Hu, X. Lu, J. Luo, W. Li, Graphene regulated ceramic electrolyte for solid-state sodium metal battery with superior electrochemical stability, ACS Appl. Mater. Interfaces 11 (2019) 5064–5072.

[49] B. He, A. Ye, S. Chi, P. Mi, Y. Ran, L. Zhang, X. Zou, B. Pu, Q. Zhao, Z. Zou, CAVD, towards better characterization of void space for ionic transport analysis, Sci. Data 7 (2020) 153.

[50] J. Kim, S. Kang, K. Min, Screening platform for promising Na superionic conductors for Na-ion solid-state electrolytes, ACS Appl. Mater. Interfaces 15 (2023) 41417–41425.

[51] B. Ouyang, J. Wang, T. He, C.J. Bartel, H. Huo, Y. Wang, V. Lacivita, H. Kim, G. Ceder, Synthetic accessibility and stability rules of NASICONs, Nat. Commun. 12 (2021) 5752.

[52] Y. Zhang, T. Zhan, Y. Sun, L. Lu, B. Chen, Revolutionizing solid-state NASICON sodium batteries: enhanced ionic conductivity estimation through multivariate experimental parameters leveraging machine learning, ChemSusChem 17 (2024) e202301284.

[53] P. Zhou, Z. Zhao, K. Sun, Q. Zhao, F. Xiao, Y. Fu, H.F. Li, Machine learning guided cobalt-doping strategy for solid-state NASICON electrolytes, Eur. J. Inorg. Chem. 26 (2023) e202300382.

[54] T. Krauskopf, R. Dippel, H. Hartmann, K. Peppler, B. Mogwitz, F.H. Richter, W. G. Zeier, J. Janek, Lithium-metal growth kinetics on LLZO garnet-type solid electrolytes, Joule 3 (2019) 2030–2049.

[55] Q. Tu, T. Shi, S. Chakravarthy, G. Ceder, Understanding metal propagation in solid electrolytes due to mixed ionic-electronic conduction, Matter 4 (2021) 3248–3268.

[56] Z. Wu, S. He, C. Zheng, J. Gan, L. She, M. Zhang, Y. Gao, Y. Yang, H. Pan, Fabrication pressures and stack pressures in solid-state battery, eScience (2024) 100247.

[57] T. Ortmann, S. Burkhardt, J.K. Eckhardt, T. Fuchs, Z. Ding, J. Sann, M. Rohnke, Q. Ma, F. Tietz, D. Fattakhova-Rohlfing, Kinetics and pore formation of the sodium metal anode on NASICON-type $Na_{3.4}Zr_2Si_{2.4}P_{0.6}O_{12}$ for sodium solid-state batteries, Adv. Energy Mater. 13 (2023) 2202712.

[58] Z. Ding, Y. Tang, V.S.K. Chakravadhanula, Q. Ma, F. Tietz, Y. Dai, T. Scherer, C. Kübel, Exploring the influence of focused ion beam processing and scanning electron microscopy imaging on solid-state electrolytes, Microscopy 72 (2023) 326–335.